

AD-A111 690

AEROSPACE CORP EL SEGUNDO CA SPACE SCIENCES LAB

F/G 4/1

ATMOSPHERIC PRESSURE AND VELOCITY FLUCTUATIONS NEAR THE AURORAL--ETC(U)

JAN 82 J G LUHMANN

F04701-81-C-0082

UNCLASSIFIED

TR-0082(2940-05)-2

SD-TR-81-105

NL

1 1 1
OF 1 40

1

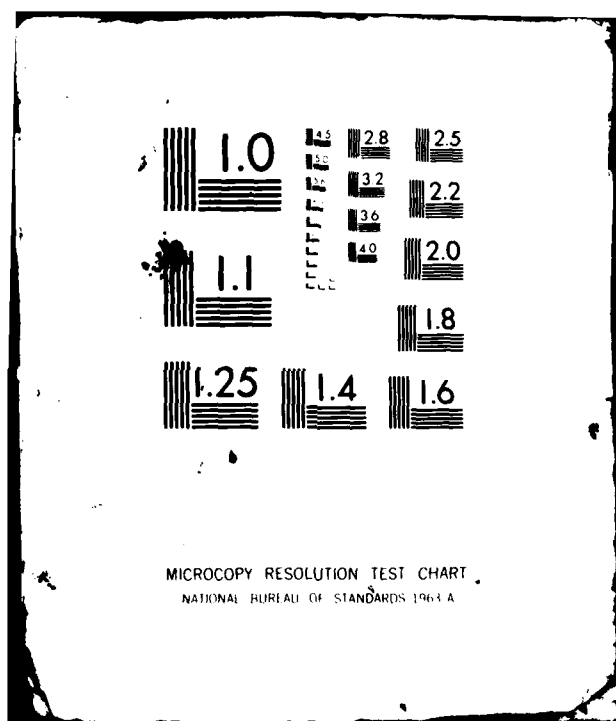
END

DATE

FILED

3 82

DTIC



12

ADA111640

Atmospheric Pressure and Velocity Fluctuations Near the Aural Electrojet

J. G. LUHMANN
Space Sciences Laboratory
Laboratory Operations
The Aerospace Corporation
El Segundo, Calif. 90245

15 January 1982

APPROVED FOR PUBLIC RELEASE;
DISTRIBUTION UNLIMITED

Prepared for
SPACE DIVISION
AIR FORCE SYSTEMS COMMAND
Los Angeles Air Force Station
P.O. Box 6000, Weapons Postal Center
Los Angeles, Calif. 90008

DTIC
ELECTRIC
MAR 4

DTIC FILE COPY

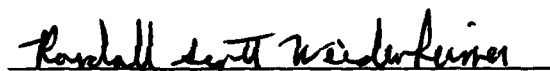
fw


82 03 04 037

This report was submitted by The Aerospace Corporation, El Segundo, CA 90245, under Contract No. F04701-81-C-0082 with the Space Division, Deputy for Technology, P.O. Box 92960, Worldway Postal Center, Los Angeles, CA 90009. It was reviewed and approved for The Aerospace Corporation by G. A. Paulikas, Director, Space Sciences Laboratory. Lt Randall S. Weidenheimer, SD/YLVS, was the project officer for Mission Oriented Investigation and Experimentation (MOIE) Programs.


This report has been reviewed by the Public Affairs Office (PAS) and is releasable to the National Technical Information Service (NTIS). At NTIS, it will be available to the general public, including foreign nations.

This technical report has been reviewed and is approved for publication. Publication of this report does not constitute Air Force approval of the report's findings or conclusions. It is published only for the exchange and stimulation of ideas.


Randall S. Weidenheimer, 2nd Lt, USAF
Project Officer


Florian P. Meinhardt, Lt Col, USAF
Director of Advanced Space Development

FOR THE COMMANDER


Norman W. Lee, Jr., Colonel, USAF
Deputy for Technology

UNCLASSIFIED

SECURITY CLASSIFICATION OF THIS PAGE (When Data Entered)

REPORT DOCUMENTATION PAGE		READ INSTRUCTIONS BEFORE COMPLETING FORM
1. REPORT NUMBER SD-TR-81-105	2. GOVT ACCESSION NO. AD-A111	3. RECIPIENT'S CATALOG NUMBER 640
4. TITLE (and Subtitle) ATMOSPHERIC PRESSURE AND VELOCITY FLUCTUATIONS NEAR THE AURORAL ELECTROJET		5. TYPE OF REPORT & PERIOD COVERED
		6. PERFORMING ORG. REPORT NUMBER TR-0082(2940-05)-2
7. AUTHOR(s) Janet G. Luhmann		8. CONTRACT OR GRANT NUMBER(s) F04701-81-C-0082
9. PERFORMING ORGANIZATION NAME AND ADDRESS The Aerospace Corporation El Segundo, Calif. 90245		10. PROGRAM ELEMENT, PROJECT, TASK AREA & WORK UNIT NUMBERS
11. CONTROLLING OFFICE NAME AND ADDRESS Space Division Air Force Systems Command Los Angeles, Calif. 90009		12. REPORT DATE 15 January 1982
		13. NUMBER OF PAGES 40
14. MONITORING AGENCY NAME & ADDRESS (if different from Controlling Office)		15. SECURITY CLASS. (of this report) Unclassified
		15a. DECLASSIFICATION/DOWNGRADING SCHEDULE
16. DISTRIBUTION STATEMENT (of this Report) Approved for public release; distribution unlimited		
17. DISTRIBUTION STATEMENT (of the abstract entered in Block 20, if different from Report)		
18. SUPPLEMENTARY NOTES		
19. KEY WORDS (Continue on reverse side if necessary and identify by block number) Atmosphere Pressure Variations Auroral Electrojet		
20. ABSTRACT (Continue on reverse side if necessary and identify by block number) The low frequency pressure and velocity perturbations caused by the temporally varying Lorentz force associated with auroral electrojet activity are modelled by calculating the disturbances generated by a two-dimensional, time-dependent current system in a gravitationally stratified, isothermal, windless atmosphere. These calculations provide information about the pattern of gravity waves around the hypothetical electrojet and give estimates of the magnitudes of near-field auroral disturbances in the middle		

DD FORM 1473
(FACSIMILE)

UNCLASSIFIED

SECURITY CLASSIFICATION OF THIS PAGE (When Data Entered)

UNCLASSIFIED

SECURITY CLASSIFICATION OF THIS PAGE(When Data Entered)

19. KEY WORDS (Continued)

20. ABSTRACT (Continued)

atmosphere. It is suggested that the near-field vertical wind shears may be large enough to affect the development of air turbulence in the auroral zone.

UNCLASSIFIED

SECURITY CLASSIFICATION OF THIS PAGE(When Data Entered)

PREFACE

The author benefited from discussions with Y. T. Chiu, D. J. Boucher, J. M. Straus, R. Waltersheid, G. Pihos, G. C. Reid, M. C. Kelley, B. B. Balsley, R. R. Vondrak, J. F. Vickrey, W. L. Ecklund and A. D. Richmond.



Accession For	
DTIS GRA&I	<input checked="checked" type="checkbox"/>
DTIC TAB	<input type="checkbox"/>
Unannounced	<input type="checkbox"/>
Justification	
By _____	
Distribution/	
Availability Codes	
Dist	Avail and/or
A	Special

CONTENTS

PREFACE	1
INTRODUCTION	7
THEORY	7
COMPUTATIONAL RESULTS AND DISCUSSION	21
QUALIFICATIONS AND CONCLUDING REMARKS	35
REFERENCES	37

FIGURES

1.	Auroral Electrojet Model Assumed in Calculation	13
2.	Time Histories of Pressure Perturbation at Various Altitudes and Ranges from Electrojet Described in Text	22
3.	Calculated Patterns of Pressure Perturbation Around Model Electrojet at Three Different Times	24
4.	Calculated Near-Field Pressure Perturbation at $t = 60$ min	25
5.	Calculated Pressure Pattern with Earth-Reflected Component Added for the Case $\alpha = (30 \text{ min})^{-1}$, $t = 60$ min	26
6.	Altitude Profiles of Horizontal Wind Velocity Perturbation by Model Electrojet at Ranges $x = 20$ km and $x = 100$ km Calculated from eq. (44) for $t = 60$ min, $\alpha = (30 \text{ min})^{-1}$ (a) and $\alpha = (300 \text{ min})^{-1}$ (b)	28
7.	Time Histories of Velocity Perturbations at Several Ranges	29
8.	Altitude Profiles of Horizontal Wind Shear Corresponding to Cases Shown in Fig. 6 as Calculated from eq. (46): (a) $\alpha = (30 \text{ min})^{-1}$; (b) $\alpha = (300 \text{ min})^{-1}$	30
9.	Time Histories of Shear Perturbations at Several Ranges	31
10.	(a) Approximate Altitude Dependence of Square of Brunt-Vaisala Frequency, (b) Velocity Shear Perturbation of Fig. 8b, and (c) Value of R_i Calculated from These quantities	34

INTRODUCTION

Dynamical perturbations of the auroral zone atmosphere by auroral activity have been observed at large distances from the auroral zone as low frequency traveling ionospheric disturbances (TIDs), (Davis, 1971) and locally as auroral infrasonic signals (AIWs) (Wilson, 1975). Theoretical descriptions of the forementioned effects have been considered by Chimonas and Hines (1970), Chimonas (1970) and Chimonas and Peltier (1970). Additional analyses emphasizing various aspects of the atmosphere's dynamical response to auroral activity have been carried out by Blumen and Hendl (1969), Testud (1970), Francis (1974), Chiu (1976), and Richmond and Matsushita (1975). Most of these authors have concentrated on the far-field disturbance with the exception of Chimonas (1970), who dealt with the infrasonic wave field near a pulsating aurora, and Richmond and Matsushita (1975) who were primarily concerned with modeling the global scale thermospheric (> 80 km altitude) response to magnetic substorms. This paper describes a theoretical investigation of atmospheric dynamics in the immediate vicinity of a transient auroral electrojet. The method of analysis is similar to that used by Chimonas and Hines (1970) in a study related to the interpretation of midlatitude TIDs except that the far-field approximation is not invoked. The results, obtained by a combination of analytical and numerical methods, are used to estimate the magnitude of the pressure, velocity and velocity shear perturbations in the atmosphere below the electrojet.

THEORY

Following Chimonas and Hines (1970), the atmosphere is treated as a compressible fluid upon which the electrojet acts as a perturbing force. Although both Joule heating and Lorentz forces contribute to the latter, it will be assumed, on the basis of several recent studies (Hunsucker, 1977, Brekke, 1978), that the Lorentz source is dominant. The atmosphere is assumed isothermal, windless and nonviscous.

The standard fluid equations that are invoked for the present analysis are continuity

$$\frac{\partial \rho}{\partial t} + \nabla \cdot (\rho \bar{V}) = 0 \quad (1)$$

Momentum

$$\rho \frac{\partial \bar{V}}{\partial t} + \rho \bar{V} \cdot \nabla \bar{V} - \rho g + \nabla p = \rho \bar{F} \quad (2)$$

and heating (neglecting the Joule source)

$$\frac{\partial}{\partial t} (p \rho^{-\gamma}) + \bar{V} \cdot \nabla (p \rho^{-\gamma}) = 0 \quad (3)$$

where ρ is the mass density, p is the pressure, \bar{V} is the fluid velocity, g is the gravitational acceleration, and γ is the ratio of specific heats. The above notation has been chosen to conform to that used by Chimonas and Hines (1970). The Lorentz force per unit mass $\bar{F} = \bar{J} \times \bar{B} / \rho$, where \bar{J} is the electrojet current and \bar{B} is the magnetic field, is communicated by the moving ions to the neutral fluid by collisions. A rectangular coordinate system is chosen in which the z axis is vertical, x is in the north-south direction, and y is in the east-west direction.

Under the assumption that the unperturbed atmospheric density $\rho_0(z)$ and pressure $p_0(z)$ are proportional to $e^{-z/H}$ where H is the constant scale height, the fluid equations (1) - (3) can be linearized and Fourier transformed in time to yield the set

$$i\omega \tilde{\rho} - \tilde{V}_z/H + \nabla \cdot \tilde{\mathbf{V}} = 0 \quad (4)$$

$$i\omega \tilde{\mathbf{V}} + gH \nabla \tilde{p}_1 + (\tilde{p}_1 - \tilde{\rho}_1) \bar{\mathbf{g}} = \tilde{\mathbf{F}} \quad (5)$$

$$i\omega \tilde{p}_1 - \tilde{V}_z/H + \gamma \nabla \cdot \tilde{\mathbf{V}} = 0 \quad (6)$$

where the \sim over the symbol denotes the transformed quantity,

$$f(t) = \frac{1}{2\pi} \int_{-\infty}^{\infty} d\omega e^{i\omega t} \tilde{f}(\omega) \quad (7)$$

and the subscripts 1 signify normalized perturbations of the form $\frac{(p - p_0)}{p_0}$.

Pressure Perturbation:

Equations (4) - (6) combine to give an equation for p_1 analogous to eq. (12) of Chimonas and Hines:

$$\nabla^2 \tilde{p}_1 + \frac{\omega_g^2}{(\omega^2 - \omega_g^2)} \frac{\partial \tilde{p}_1}{\partial z^2} - \frac{\omega^2}{(\omega^2 - \omega_g^2)H} \frac{\partial \tilde{p}_1}{\partial z}$$

$$+ \frac{\omega^4}{(\omega^2 - \omega_g^2) + \omega_A^2 H^2} \tilde{p}_1 = \frac{1}{gH} \nabla \cdot \tilde{F} \quad (8)$$

where $\omega_A = 1/2 \sqrt{\gamma g/H}$ is the acoustic cut-off frequency and $\omega_g = \sqrt{(\gamma - 1)g/\gamma H}$ is the Brunt - Vaisala frequency. As pointed out by these authors, the substitution

$$\tilde{p}_1 = e^{z/2H} \phi(x, z) \quad (9)$$

reduces eq. (8) to the form

$$\frac{\partial \phi}{\partial x^2} + A_1 \frac{\partial \phi}{\partial z^2} + A_2 \phi = M_1 \quad (10)$$

where

$$A_1 = \frac{\omega^2}{(\omega^2 - \omega_g^2)} \quad (11)$$

$$A_2 = \frac{\omega^2}{C^2} \frac{(\omega^2 - \omega_A^2)}{(\omega^2 - \omega_g^2)} \quad (12)$$

$$C^2 = \gamma gH \quad (13)$$

and

$$M_1 = e^{-z/2H} \frac{\partial \tilde{F}_x}{\partial x} / gH \quad (14)$$

The procedure for solving eq. (10) used here differs somewhat from that employed by Chimonas and Hines. First, it is assumed that the electrojet flows in the east-west direction and that it can be described by the current

$$\bar{J} = \hat{y} A f(z) g(x) T(t) \quad (15)$$

In this case the Lorentz force for a vertical B field gives a form for M_1 given by

$$M_1 = Q \mathcal{L}(z) G(x) \tilde{T}(w) \quad (16)$$

where

$$Q = \frac{BA}{gH} \quad (17)$$

$$\mathcal{L}(z) = e^{-z/2H} \frac{f(z)}{\rho(z)} \quad (18)$$

$$G(x) = \frac{dg(x)}{dx} \quad (19)$$

Two successive Fourier transformations of eq. (10) in the spatial variables x and z then lead to the equation

$$(-k_x^2 - A_1 k_z^2 + A_2) \tilde{\phi} = Q \tilde{\mathcal{L}}(k_z) \tilde{G}(k_x) \tilde{T}(w) \quad (20)$$

Equation (20) can be solved for an infinite atmosphere if the functions used in the description of the electrojet current are carefully chosen. The model selected for the present analysis is shown in Fig. 1. If a box function is selected to represent the sharp north-south boundary of an auroral electrojet:

$$g(x) = \begin{cases} 0 & x < \eta \\ 1 & \eta < x < \eta + \sigma \\ 0 & x > \eta + \sigma \end{cases} \quad (21)$$

then $\tilde{G}(x) = \frac{dg(x)}{dx} = \delta(x - \eta) - \delta(x - \eta - \sigma)$ (22)

and the x dependence of the right hand side of eq. (20) is contained in the transformed function

$$\tilde{G}(k_x) = -i(e^{ik_x \eta} - e^{ik_x(\eta + \sigma)})/k_x \quad (23)$$

It follows that the Fourier inversion in x gives

$$\tilde{\phi} = Q \tilde{f}(k_z) \tilde{T}(\omega) \frac{1}{\omega_0} \left[\sin \omega_0(x - \eta) - \sin \omega_0(x - \eta - \sigma) \right] \quad (24)$$

where $\omega_0 = \left[-A_1 k_z^2 + A_2 \right]^{1/2}$ (25)

If the altitude dependence of M_1 is approximated by

$$\mathcal{L}(z) = e^{-z/2H} \frac{f(z)}{\rho(z)} = \begin{cases} 0 & z < \xi \\ 1/\rho_0(0) & \xi < z < \xi + \lambda \\ 0 & z > \xi + \lambda \end{cases} \quad (26)$$

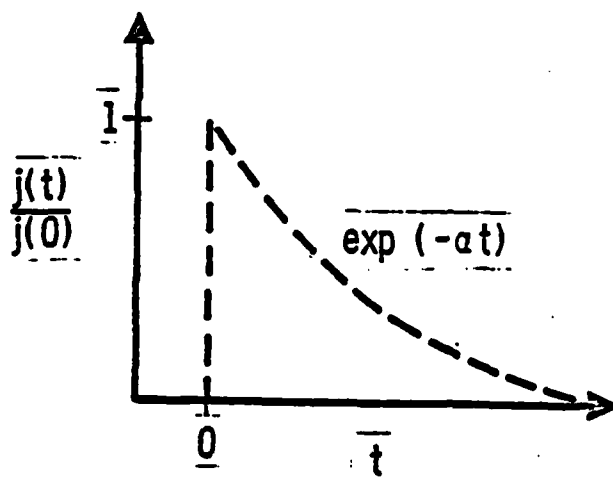
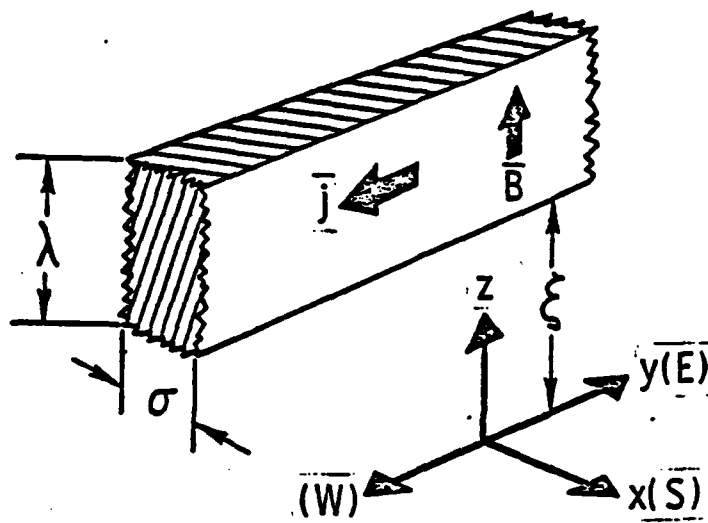


Fig. 1. Auroral Electrojet Model Assumed in Calculation.

the inversion in z , performed with the aid of the convolution theorem (eg. see Butkov, 1968) gives

$$\phi = \frac{-Q \tilde{T}(\omega)}{\rho_0(0)} \frac{1}{\sqrt{-A_1}} \int_{\xi}^{\xi+\lambda} ds [J_0(X_1) - J_0(X_2)] \quad (27)$$

in which the arguments of the zero order Bessel functions J_0 are

$$X_1 = \sqrt{\frac{-A_2}{A_1}} \left(-A_1 (x - \eta)^2 - (z - s)^2 \right)^{1/2} \quad (28)$$

and

$$X_2 = \sqrt{\frac{-A_2}{A_1}} \left(-A_1 (x - \eta - \sigma)^2 - (z - s)^2 \right)^{1/2} \quad (29)$$

A final inverse transformation is needed to obtain the fractional pressure pulse from ϕ :

$$p_1(x, z, t) = \frac{1}{\sqrt{2\pi}} \int_{-\infty}^{\infty} \tilde{p}_1 e^{i\omega t} d\omega = \frac{e^{z/2H}}{\sqrt{2\pi}} \int_{-\infty}^{\infty} \phi e^{i\omega t} d\omega \quad (30)$$

The inverse transform of the Bessel function in the integrand of eq. (27) can be found in tables for the low frequency ($\omega \ll \omega_g$) limit since the approximations

$$A_1 \approx -\frac{\omega^2}{\omega_g^2} \quad \text{and} \quad A_2 \approx -A_1 \frac{\omega_A^2}{\omega_g^2} \quad (31)$$

can be made. The arguments (eqs (28) and (29)) then take the form $b(\omega^2 - a^2)^{1/2}$, in which case the inverse is

$$\int_{-\infty}^{\infty} d\omega e^{i\omega t} J_0(b(\omega^2 - a^2)^{1/2}) = \begin{cases} 0 & t < b \\ \frac{4i \cos(a(t^2 - b^2)^{1/2})}{(t^2 - b^2)^{1/2}} & t > b \end{cases} \quad (32)$$

If the inverse transform of $\tilde{T}(\omega)/\omega$ can be found, the convolution theorem can be used once again to evaluate the low frequency response for eq. (30). The function $T(t) = e^{-at} S(t)$, shown in Fig. 1, bears a reasonable resemblance to the temporal behavior of an auroral storm and gives an imaginary transform for $\tilde{T}(\omega)/\omega$ of the form

$$\text{Im} \int_{-\infty}^{\infty} d\omega e^{i\omega t} \frac{\tilde{T}(\omega)}{\omega} = \frac{2\pi}{a} e^{-at} \quad (33)$$

The convolution theorem subsequently leads to:

$$p_1(x, z, t) = \frac{Q\omega_g e^{z/2H}}{\rho_0(0) a} \left[\int_{b_1}^t d\tau \int_{\xi}^{\xi + \lambda} ds e^{-a(t - \tau)} \right] \quad (34)$$

$$\left\{ \cos \left[\frac{\omega_g(z-s)}{(x-n)} \left(\tau^2 - \left(\frac{\omega_A}{C\omega_g} (x-\eta) \right)^2 \right)^{1/2} \right] / \left(\tau^2 - \left(\frac{\omega_A}{C\omega_g} (x-\eta) \right)^2 \right)^{1/2} \right\} -$$

$$\int_{b_2}^t d\tau \int_{\xi}^{\xi + \lambda} ds e^{-a(t-\tau)} \left\{ \cos \left[\frac{\omega_g(z-s)}{(x-\eta-\sigma)} \left(\tau^2 - \left(\frac{\omega_A}{C\omega_g} (x-\eta-\sigma) \right)^2 \right)^{1/2} \right] / \right. \\ \left. \left(\tau^2 - \left(\frac{\omega_A}{C\omega_g} (x-\eta-\sigma) \right)^2 \right)^{1/2} \right\}$$

$$\text{for } b_1 = \left| \frac{\omega_A}{C\omega_g} (x-\eta) \right| \quad (35)$$

$$\text{and } b_2 = \left| \frac{\omega_A}{C\omega_g} (x-\eta-\sigma) \right| \quad (36)$$

The integration over s can be done analytically:

$$P_1(x, z, t) = \frac{Q \omega_g e^{z/2H}}{\rho_0(0) a} \left[\int_{b_1}^t d\tau e^{-a(t-\tau)} \right.$$

$$\left. \left\{ \left[\sin B_1 (\xi + \lambda - z) - \sin B_1 (\xi - z) \right] / \left(B_1^2 \frac{(x-\eta)}{\omega_g} \right) \right\} - \right. \quad (37)$$

$$\left. \int_{b_2}^t d\tau e^{-a(t-\tau)} \left\{ \left[\sin B_2 (\xi + \lambda - z) - \sin B_2 (\xi - z) \right] / \left(B_2^2 \frac{(x-\eta-\sigma)}{\omega_g} \right) \right\} \right]$$

Here B_1 and B_2 are given by

$$B_1 = \left(\tau^2 - \left(\frac{\omega_A}{C \omega_g} (x - \eta) \right)^2 \right)^{1/2} \frac{\omega_g}{(x - \eta)} \quad (38)$$

and

$$B_2 = \left(\tau^2 - \left(\frac{\omega_A}{C \omega_g} (x - \eta - \sigma) \right)^2 \right)^{1/2} \frac{\omega_g}{(x - \eta - \sigma)} \quad (39)$$

The remaining integration over τ must be carried out numerically.

Velocity perturbation:

Because the ω transform of the horizontal velocity perturbation u is related to the transform of the pressure perturbation by the momentum equation (5):

$$\tilde{u}(x, z, \omega) = - \frac{1}{i\omega} \left[Hg \frac{\partial \tilde{P}_1}{\partial x} - \tilde{F} \right] \quad (40)$$

a differential equation for u analogous to eq. (10) can be written:

$$\frac{\partial^2 \Xi}{\partial x^2} + A_1 \frac{\partial^2 \Xi}{\partial z^2} + A_2 \Xi = M_2 \quad (41)$$

where

$$\Xi = e^{-z/2H} \tilde{u} \quad (42)$$

and

$$M_2 = - \frac{H_g}{i\omega} \frac{\partial M_1}{\partial x} \quad (43)$$

for the domain outside of the range $\eta < x < \eta + \sigma$ directly beneath the electrojet. Proceeding as in the calculation of the pressure perturbation, a solution is obtained by the use of Fourier transforms;

$$u(x, z, t) = \frac{Q' \omega_g e^{z/2H}}{\rho_0(0) a^2} \quad (44)$$

$$\left[\int_{b_1}^t d\tau \right] \left[e^{-a(t-\tau)} - 2a(t-\tau) \right] \left[\cos B_1(\xi + \lambda - z) - \cos B_1(\xi - z) \right] / \left(B_1(x - \eta) / \omega_g \right) \left\{ \right. \\ \left. - \int_{b_2}^t d\tau \left\{ \left[e^{a(t-\tau)} - 2a(t-\tau) \right] \left[\cos B_2(\xi + \lambda - z) - \cos B_2(\xi - z) \right] / \left(B_2(x - \eta - \sigma) / \omega_g \right) \right\} \right\}$$

where

$$Q' = Q C^2 / \gamma \quad (45)$$

The corresponding vertical shear of the horizontal wind is also of interest:

$$\frac{\partial u}{\partial z}(x, z, t) = \frac{u(x, z, t)}{2H} - \frac{Q' \omega_g e^{z/2H}}{\rho_0(0) a^2}.$$

$$\begin{aligned} & \left[\int_{b_1}^t d\tau \left\{ \left[e^{-a(t-\tau)} - 2a(t-\tau) \right] \left[\sin B_1(\xi + \lambda - z) - \sin B_1(\xi - z) \right] / \right. \right. \\ & \quad \left. \left. (x - \eta) / \omega_g \right\} \right] \\ & + \int_{b_2}^t d\tau \left\{ \left[e^{-a(t-\tau)} - 2a(t-\tau) \right] \left[\sin B_2(\xi + \lambda - z) - \sin B_2(\xi - z) \right] \right. \\ & \quad \left. (x - \eta - \sigma) / \omega_g \right\} \end{aligned}$$

COMPUTATIONAL RESULTS AND DISCUSSION

Figure 2 shows some time histories of the pressure perturbation at various ranges and altitudes below the electrojet calculated from eq. (37) with the representative values $A\sigma\lambda = 10^6$ Amps, $\sigma = 12$ km, $\eta = 0$ km, $\xi = 100$ km, $\lambda = 20$ km, $H = 10^4$ m, $g = 9.5$ m sec^{-2} , $\gamma = 1.4$, $\omega_A = 1/2 \sqrt{g/H}$, $\omega_g = .017 \text{ sec}^{-1}$, $B = 6 \times 10^{-5}$ Wm^{-2} , and $\rho_0(0) = 1.2 \times 10^{-3} \text{ kg m}^{-3}$, for $\alpha = (30 \text{ min})^{-1}$ and $\alpha = (300 \text{ min})^{-1}$. Although the actual temporal behavior and spatial morphology of the electrojet are not well known (Francis, 1974), these parameters together with the model shown in Fig. 1 approximate some of the characteristics deduced from radar observations (Greenwald et al., 1973, 1975, Brekke 1978). Since the mathematical treatment was carried out for the limit of low frequencies, temporal structures with time scales > 10 min are presumably valid results. The fast transients seen in Fig. 2 are questionable features which may be related in part to high frequency components in the electrojet time structure, especially at onset (see Fig. 1). Caution must also be exercised in the application of the quasi-linear calculation at altitudes where the magnitude of the perturbation becomes comparable to the ambient pressure. Because the solution is symmetric about $z = \xi + \lambda/2$, the oscillations at $z = 10$ km can be compared with the characteristics of TIDs which are observed at an altitude of 200 km where the pressure is $\sim 10^{-6}$ mb. Chimonas and Hines (1970) imply that typical ~ 1 hr period perturbations of a few percent are seen 3000 km equatorward of the auroral zone, consistent with the results shown in Fig. 2.

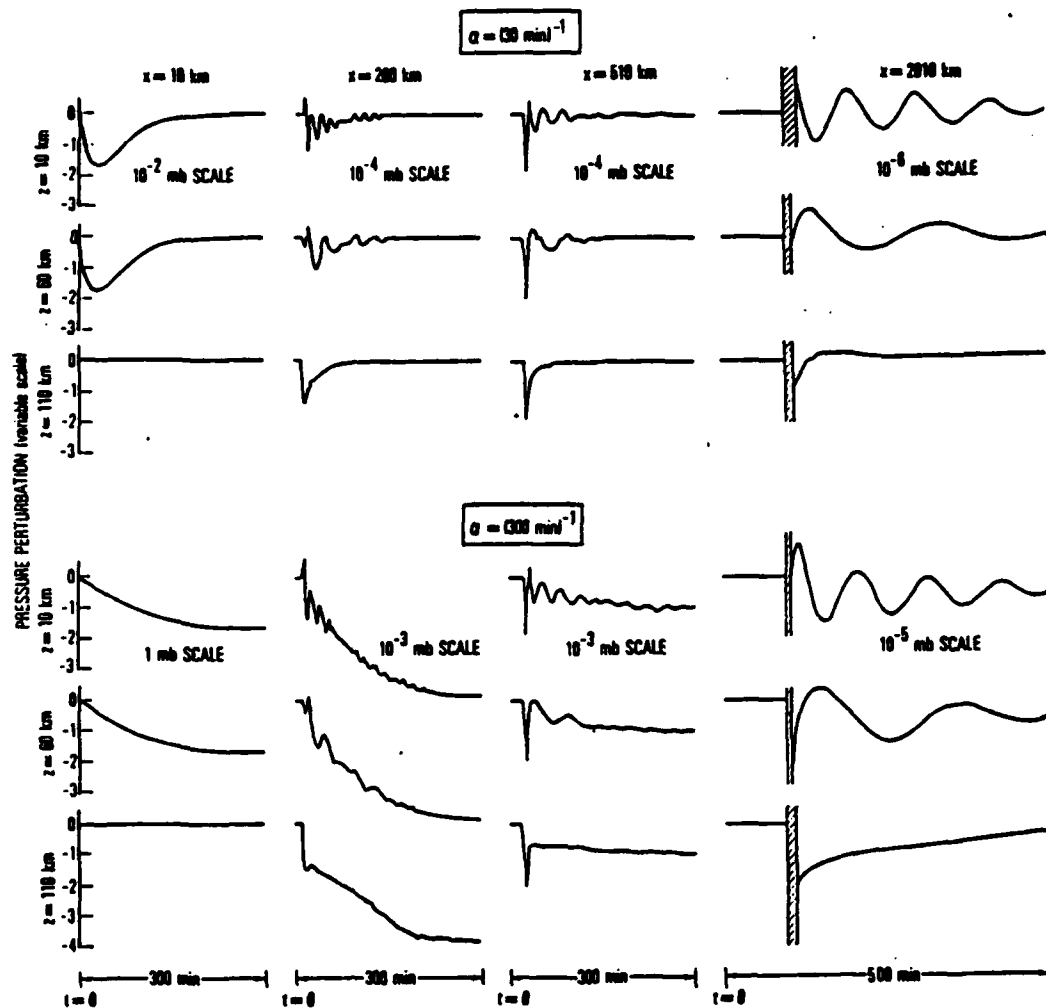


Fig. 2. Time Histories of Pressure Perturbation at Various Altitudes and Ranges from Electrojet Described in Text. Scale for $x = 2010 \text{ km}$ results is magnified to show details of oscillations that follow the initial transient. Off-scale values are indicated by cross-hatching.

Another view of the spatial and temporal development of the pressure perturbation is seen in Fig. 3 which shows how the sinusoidal oscillations, which belong to the class of gravity waves, develop at distances from the source where significant dispersion of the Fourier components occurs. This picture also illustrates the direction of phase propagation, which is normal to the direction of energy propagation from the source as expected for gravity waves (Beer, 1978). These patterns are symmetric about $z = \xi + \lambda/2$ and change sign at the source midplane $x = \eta + \sigma/2$ where the Lorentz force switches direction between toward and away from the electrojet.

An amplified view of the very near-field of the pressure perturbation is given in Fig. 4. Here, the maximum disturbance, which becomes infinite at the site of the N-S boundaries of the model electrojet ($x - \eta = 0$ and $x - \eta = \sigma$) is seen. Because the sharp vertical-edge geometry of the model is unrealistic, this behavior is an artifact; however, the nearby perturbations of ≤ 0.1 -1.0 mb may be realized in nature if the electrojet edge is fairly localized in range. Of course, a perturbation of this magnitude is too large to be considered linearly at altitudes > 50 km.

The earth reflected wave, discussed by Francis (1974) can be easily included if it is assumed to be reflected with efficiency ϵ and is describable by an image source at $z = -(\xi + \lambda/2)$:

$$P_{\text{total}} = P_1(x, z, t, \xi, \lambda) + \epsilon P_1(x, z, t, -\xi, -\lambda)$$

An example of the modification of the pressure pattern with the total ($\epsilon = 1$) reflected component added is shown in Fig. 5. It can be seen from Fig. 5 that the pressure pattern becomes more complicated, but more

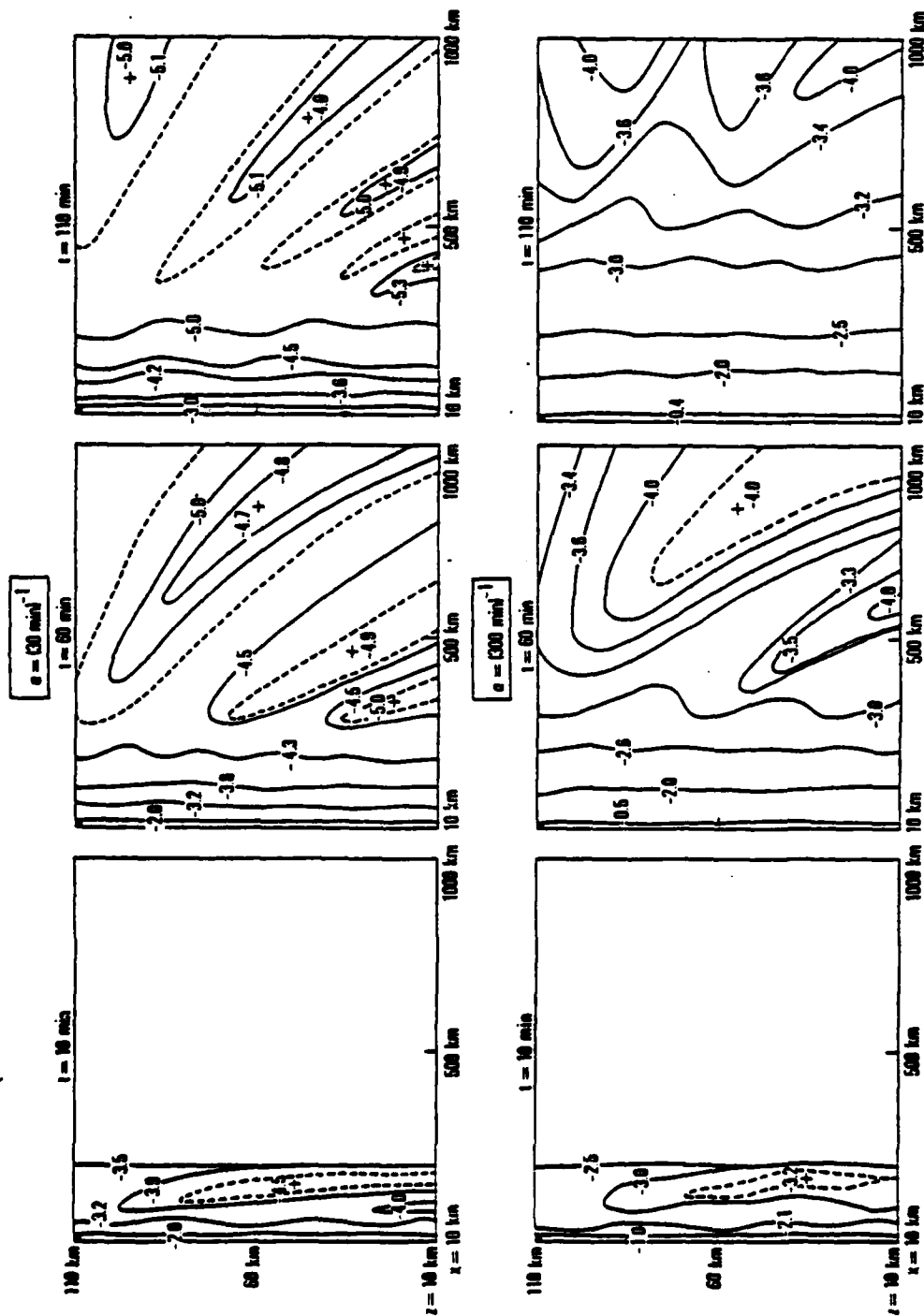


Fig. 3. Calculated Patterns of Pressure Perturbation Around Model Electrojet at Three Different Times. Electrojet is located in upper left corner. Contour labels indicate logarithm of pressure perturbation magnitude in millibars. Dashed contours show location where sign of perturbation goes through zero. Pulses identify regions of positive perturbations; regions on outside of dashed contours have negative perturbations or sub-quietest pressure. Patterns are symmetric about $z = \xi + \lambda/2$, and change sign at the electrojet mid-plane $x = \eta + \sigma/2$.

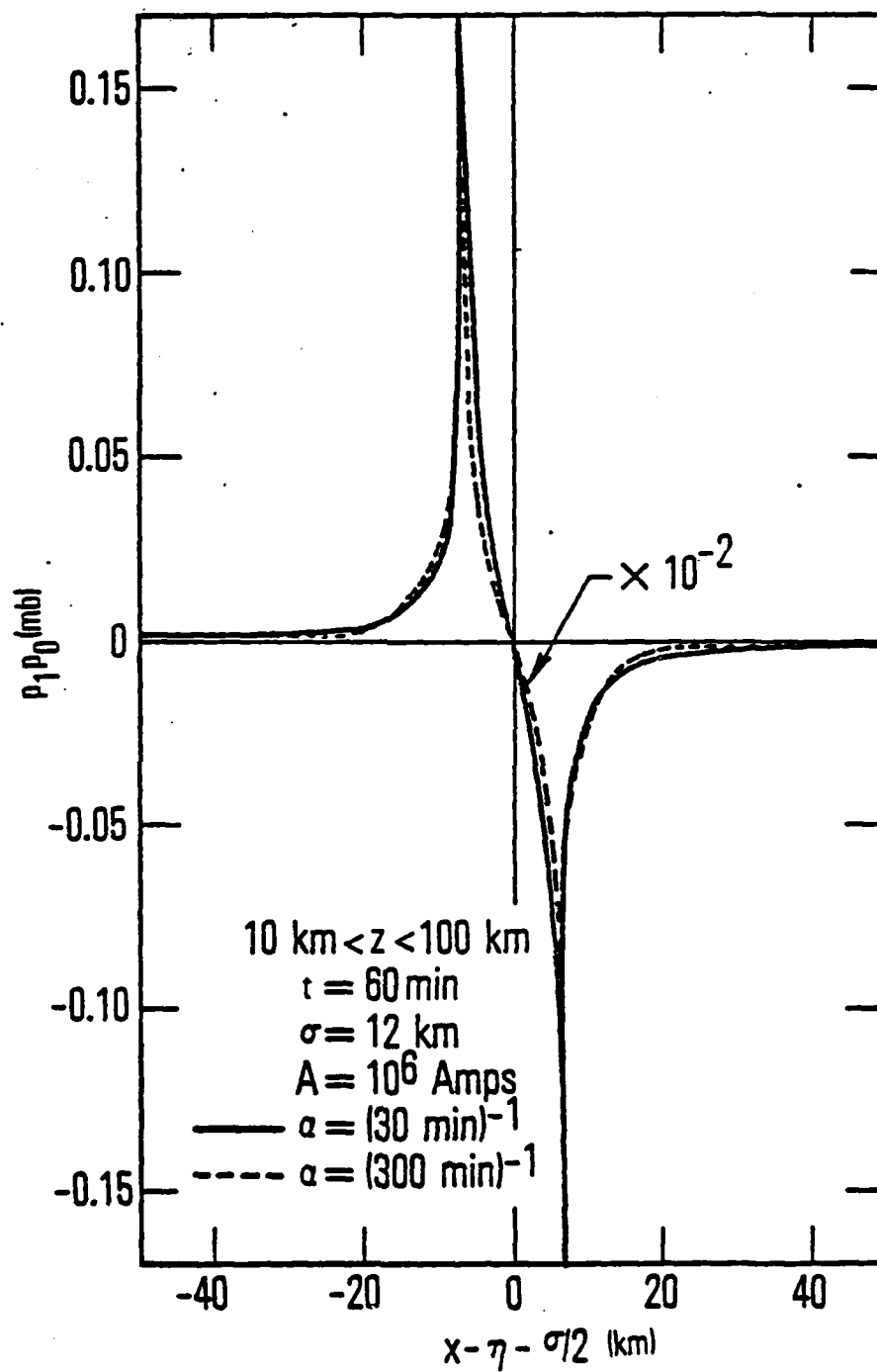


Fig. 4. Calculated Near-Field Pressure Perturbation at $t = 60 \text{ min}$.

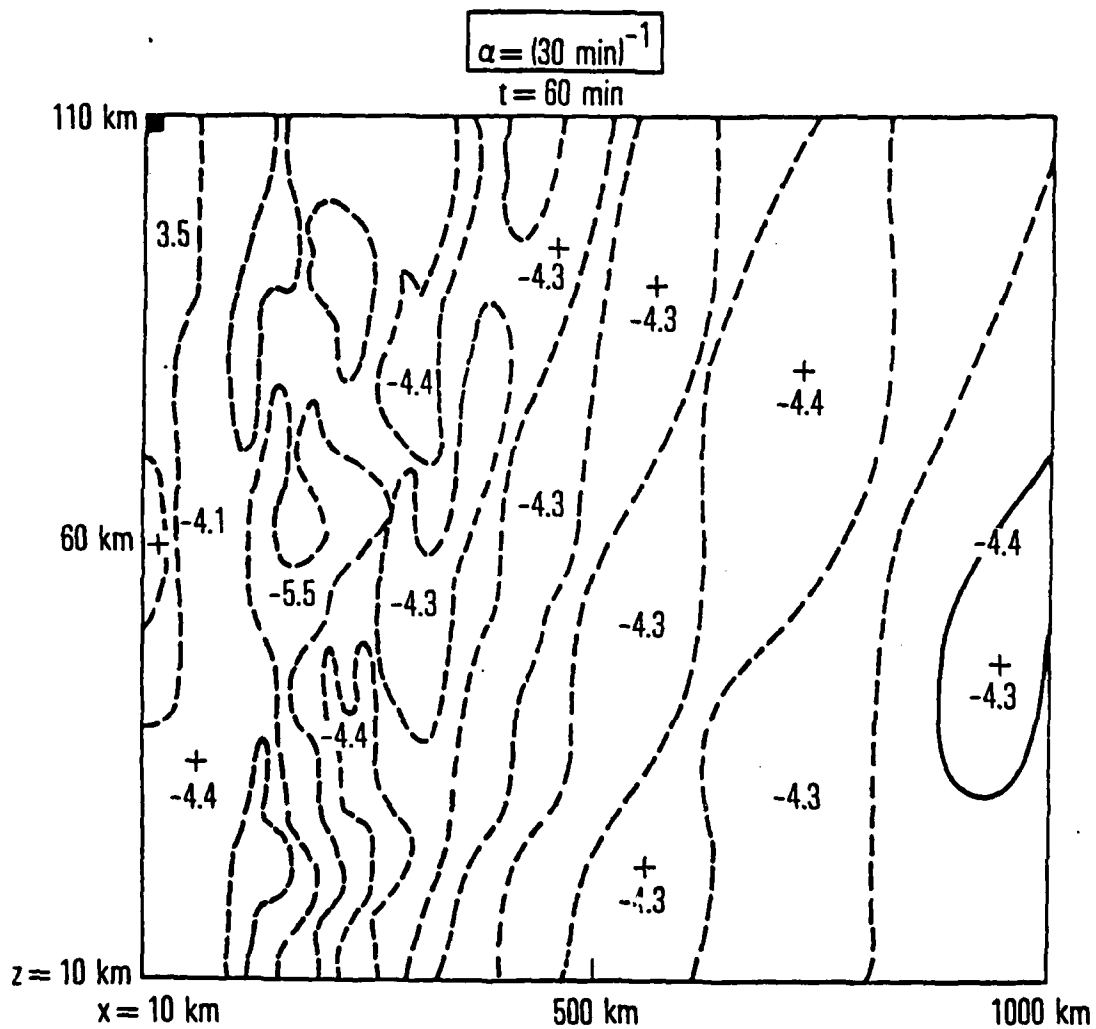


Fig. 5. Calculated Pressure Pattern with Earth-Reflected Component Added for the Case $\alpha = (30 \text{ min})^{-1}$, $t = 60 \text{ min}$. Format of this contour diagram is described in Fig. 2 caption.

importantly, that the very near-field magnitude is evidently reduced substantially by destructive interference with the direct perturbation. Since the reflection properties of the boundary layer are probably variable, Fig. 3 and Fig. 5 represent extreme cases.

The velocity perturbation described by eq. (44) is quite structured compared to the pressure perturbation and so is not easily displayed as a contour diagram. Figure 6 shows some representative altitude profiles of the velocity perturbation at two different ranges. Examples of the time histories of these perturbations for the case $\alpha = (300 \text{ min})^{-1}$ are given in Fig. 7. As noted in the discussion of the pressure perturbations that were shown in Fig. 2, rapid time scale ($\lesssim 10 \text{ min}$) fluctuations, which appear to dominate the velocity spectrum at $x = 20 \text{ km}$ where very large perturbations are seen, are of questionable validity. However, low frequency ($\omega < \omega_g$) variations of $\sim 20\text{-}30 \text{ m s}^{-1}$ are clearly present in some of the waveforms, especially at $x = 100 \text{ km}$. A more precise determination of the low frequency content of these results could in principle be obtained by a numerical Fourier analysis, but this additional computation has not been carried out at the present time. The corresponding vertical shears of the velocity can be inferred from Fig. 6 or calculated from eq. (46). The latter method produced the altitude profiles and time histories displayed in Figs. 8 and 9, respectively. Even if the high frequency component is disregarded, it is apparent that shears of up to $\sim 10 \text{ m s}^{-1}/\text{km}$ occur when the value $\alpha = (300 \text{ min})^{-1}$ is used. Not surprisingly, the long-lived auroral activity produces the stronger low frequency effects.

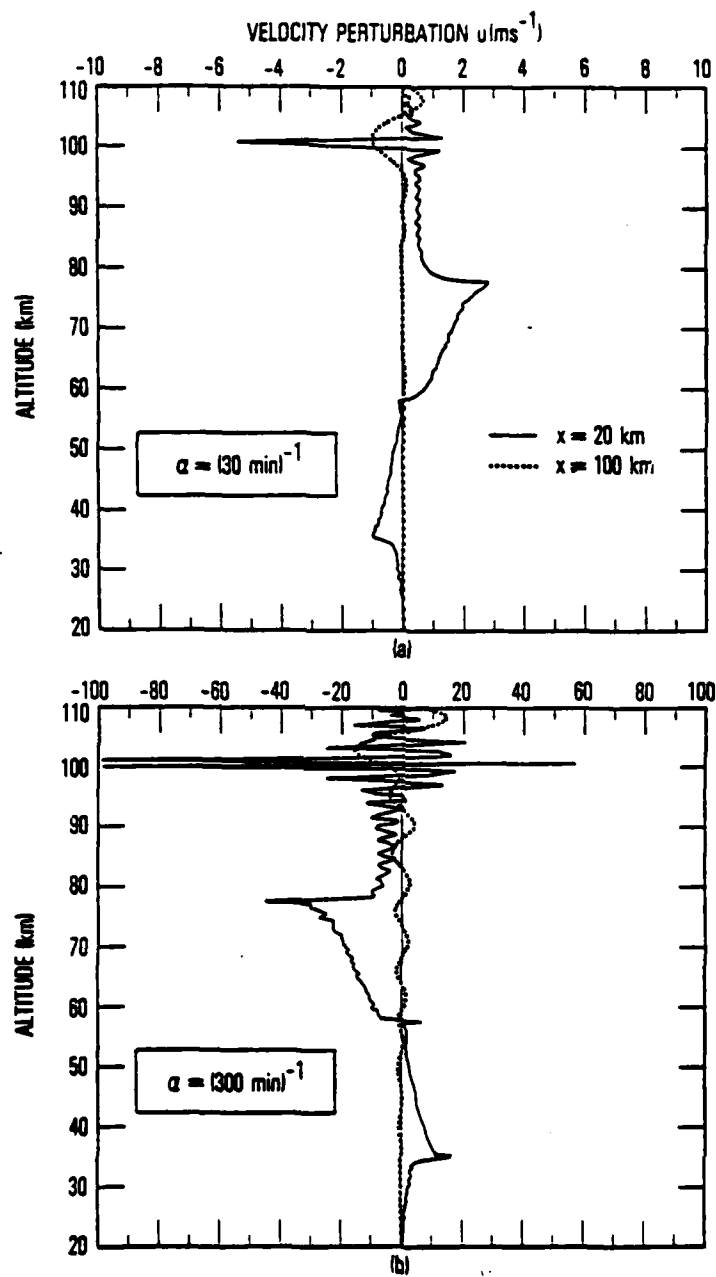


Fig. 6. Altitude Profiles of Horizontal Wind Velocity Perturbation by Model Electrojet at Ranges $x = 20 \text{ km}$ and $x = 100 \text{ km}$ Calculated from eq. (44) for $t = 60 \text{ min}$, $\alpha = (30 \text{ min})^{-1}$ (a) and $\alpha = (300 \text{ min})^{-1}$ (b). Altitude resolution is 0.5 km . Structure at $\sim 20 \text{ km}$ altitude intervals results from altitude structure of source.

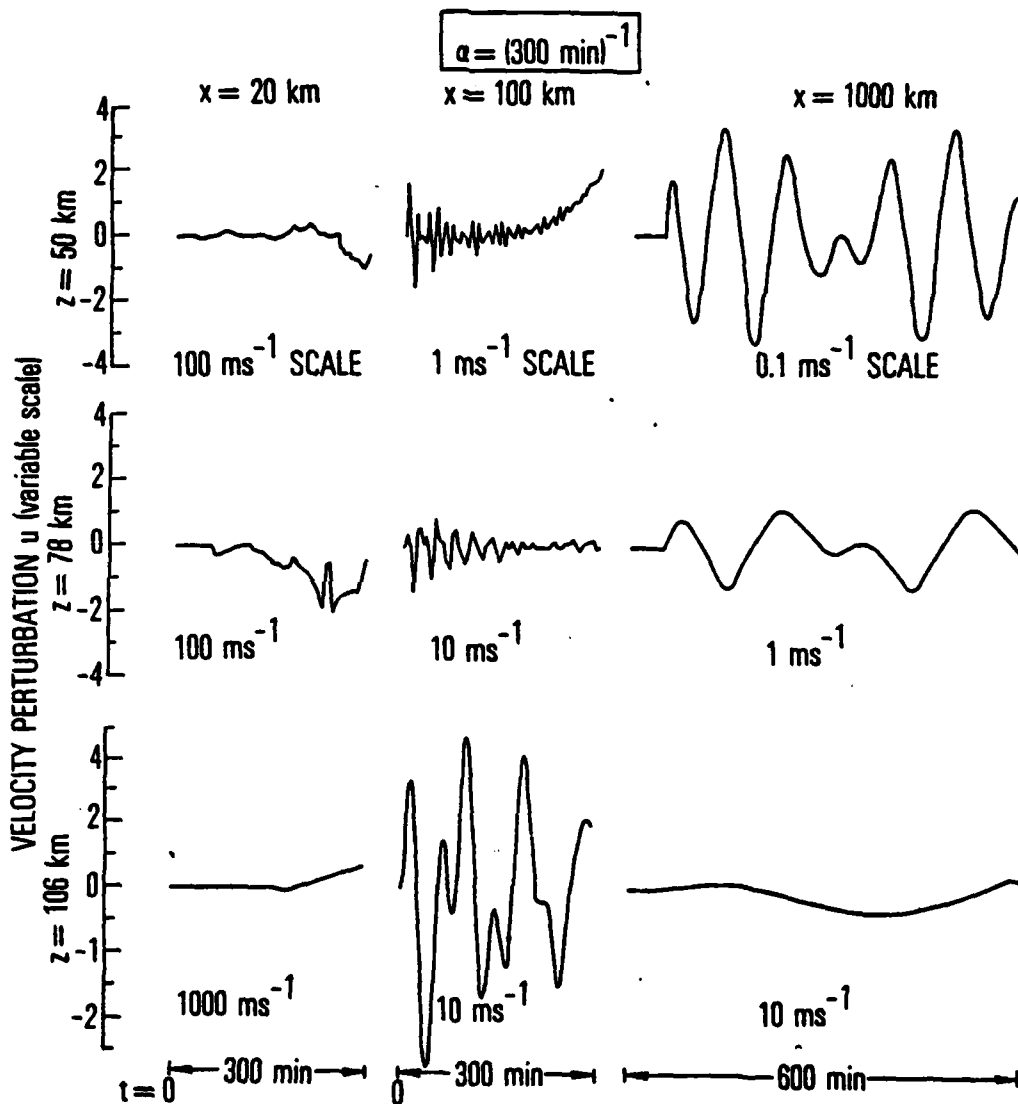


Fig. 7. Time Histories of Velocity Perturbations at Several Ranges. Temporal resolution is 5 min.

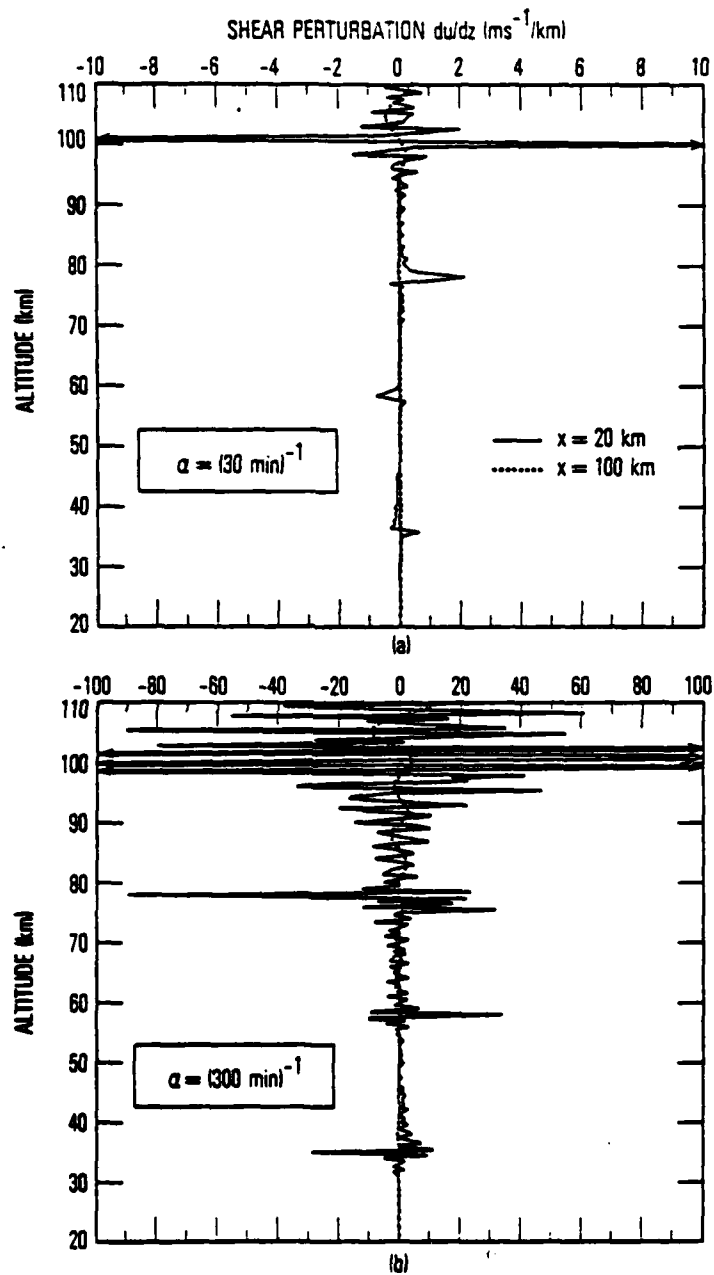


Fig. 8. Altitude Profiles of Horizontal Wind Shear Corresponding to Cases Shown in Fig. 6 as Calculated from eq. (46):
(a) $\alpha = (30 \text{ min})^{-1}$; (b) $\alpha = (300 \text{ min})^{-1}$.
Spatial resolution is 0.5 km.

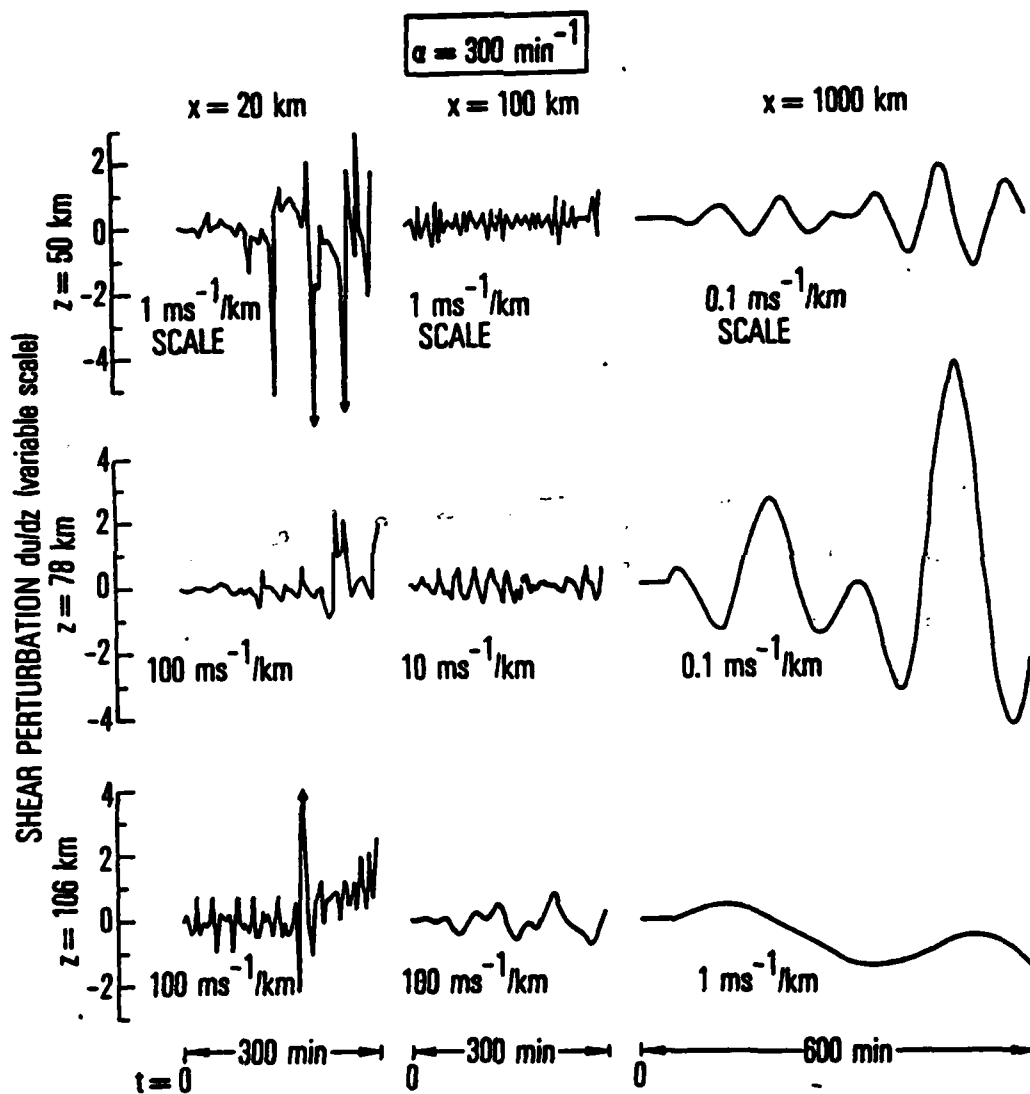


Fig. 9. Time Histories of Shear Perturbations at Several Ranges. Temporal resolution is 5 min.

At this point in the discussion, it is useful to point out that all of the above results can be rather easily extended to other electrojet current strengths and scale sizes. The former modification involves straightforward renormalization. Structured or latitudinally wider electrojet geometries produce perturbations that can be constructed from superpositions of the given patterns, appropriately shifted in latitude in accordance with the source distribution.

Among the results, velocity shears are of particular interest because they have been found to influence the potential for air turbulence at a specific location. In particular, a standard index which is used as a measure of instability is the gradient Richardson number (Woods, 1969)

$$Ri = \frac{\omega_g^2}{\left(\frac{\partial u}{\partial z}\right)^2} \quad (47)$$

Turbulence in both the ocean and the atmosphere is found to be correlated with large vertical shears in velocity and with small Richardson numbers, but the definition of the threshold or critical values appears to vary with the circumstances. For example, Waco (1970) found empirically that stratospheric clear air turbulence (CAT) was likely to occur in regions where the wind shear exceeded $\sim 2.5 \text{ m s}^{-1}/\text{km}$ and where Ri was less than 15. Unfortunately, a similar analysis for the upper middle atmosphere does not appear to have been carried out. Nevertheless, it is interesting to note that wind shears with a low frequency component of the order of the forementioned magnitude are found for the case

of the slowly decaying electrojet event if the current is reduced from 10^6 A to 10^5 A. If one conservatively adopts the velocity shear profile at $x = 100$ km from Fig. 8b, for which the low frequency content is clearly distinguishable in Fig. 9, Richardson numbers for a particular time and location in the perturbed zone can be estimated. The average magnitude of the Brunt-Vaisala frequency in the low and middle atmosphere is shown in Fig. 10a. As seen here, the actual value of ω_g is not constant, as assumed in the calculations, but varies with altitude due to the temperature structure of the atmosphere according to the formula

$$\omega_g^2 = -g \left(\frac{1}{\rho} \frac{\partial \rho}{\partial z} - \frac{g}{\gamma R T} \right) \quad (47)$$

where R is the gas constant

If it is assumed that the auroral activity affects the wind shear more than it affects ω_g , the Richardson number in the vertical cross-section corresponding to the shear perturbation of Figs. 8b and 10b is given by Fig. 10c. Layers of small Richardson number occur near the altitude of the electrojet, suggesting the possibility of upper mesosphere turbulence generation by auroral activity. Although the effects discussed above are restricted to high altitudes, it is worthwhile to note that the local minima in ω_g at the mesopause and tropopause make these regions particularly susceptible to turbulence because Ri for a particular wind shear is automatically smaller there. The addition of an ambient wind shear to the wave-induced shear could further increase the probability of CAT or alternatively suppress instability depending on whether the auroral perturbations enhance or reduce the local background shear. Of course, these inferences are based on a calculation with many potential sources of error; moreover, ω_g is probably affected by both background and aurorally induced temperature and density variations.

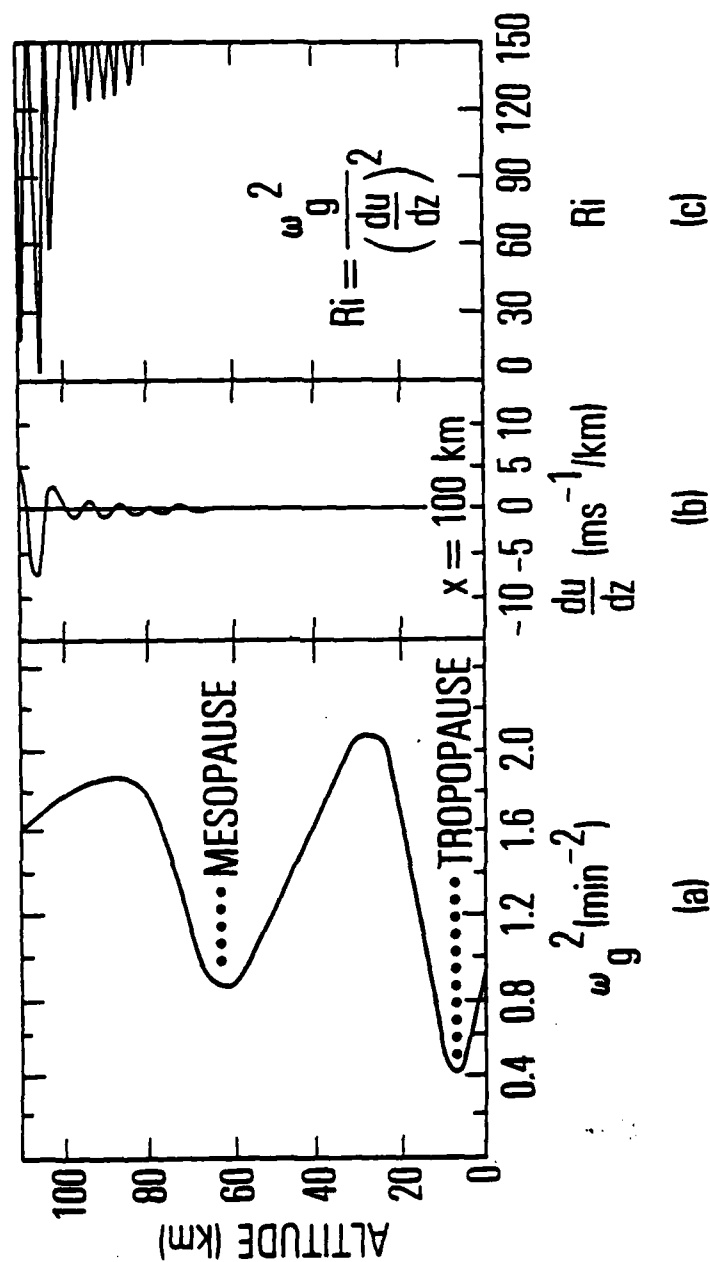


Fig. 10. (a) Approximate Altitude Dependence of Square of Brunt-Vaisala Frequency, (b) Velocity Shear Perturbation of Fig. 8b, and (c) Value of Ri Calculated from these Quantities.

QUALIFICATIONS AND CONCLUDING REMARKS

A major point of concern in the above calculations is the assumption of an isothermal atmosphere. However, Francis (1974) has argued that no strong ducting mechanisms operate for the waves considered in both his own report and here. Free propagation below 100 km altitude, with the exception of the boundary at the surface of the earth, was also assumed in that author's earlier analysis of medium scale TIDs. The full nonisothermal calculation must be carried out by methods (e.g. see Friedman, 1966) which are outside of the scope of this work. The effects of ambient winds (e.g. see Hines and Reddy, 1967) are also not incorporated in the present effort for similar reasons. Moreover, the application of linear perturbation theory here can be questioned, as discussed above, as can the credibility of the high frequency component of the calculated results. The magnitude and geometry of the assumed electrojet model may also be challenged. The sharp edges of the volume containing the current can produce unrealistic features in the solution; furthermore, substorms are often found to have electrojet currents of only 10^5 A and meridional extents of several hundred km. Thus, the calculated effects are likely to overestimate the usual situation. However, in spite of these qualifications, the present calculations seem to raise some interesting issues concerning the near-field atmospheric perturbations caused by the auroral electrojet such as the possibility of air turbulence generation in the auroral zone during severe geomagnetic storms.

REFERENCES

- Beer, T., Atmospheric Waves, John Wiley & Sons, New York, 1974.
- Blumen, W. and R. G. Hendl, On the role of Joule Heating as a source of gravity wave energy above 100 km, J. Atmos. Sci. 26, 210, 1969.
- Brekke, A., On the relative importance of Joule heating and the Lorentz force in generating atmospheric gravity waves and infrasound waves in the auroral electrojets, J. Atmos. Terr. Phys. 41, 475, 1979.
- Brekke, A. And C. L. Rino, High-resolution altitude profiles of the auroral zone energy dissipation due to ionospheric currents, J. Geophys. Res. 83, 2517, 1978.
- Chimonas, G., Infrasonic waves generated by auroral currents, Planet. Space Sci. 18, 591, 1970.
- Chimonas, G. and C. O. Hines, Atmospheric gravity waves launched by auroral currents, Planet. Space Sci. 18, 565, 1970.
- Chimonas, G. and W. R. Peltier, The bow wave generated by an auroral arc in supersonic motion, Planet. Space Sci. 18, 599, 1970.
- Chiu, Y. T., Planetary scale wave response to auroral heating of the neutral atmosphere, J. Geophys. Res. 81, 1231, 1976.
- Davis, M. J., On polar substorms as the source of large-scale traveling ionospheric disturbances, J. Geophys. Res. 76, 4525, 1971.

Francis, S. H., A theory of medium-scale traveling ionospheric disturbances, J. Geophys. Res. 79, 5245, 1974.

Friedman, J. P., Propagation of internal gravity waves in a thermally stratified atmosphere, J. Geophys. Res. 71, 1033, 1966.

Greenwald, R. A., W. L. Ecklund and B. B. Balsley, Auroral currents, irregularities and luminosity, J. Geophys. Res. 78, 8193, 1973.

Hines, C. O. and C. A. Reddy, On the propagation of atmospheric gravity waves through regions of wind shear, J. Geophys. Res. 72, 1015, 1967.

Hunsucker, R. D., Estimate of the relative importance of Joule heating and the Lorentz force in generating atmospheric gravity waves from the auroral electrojet, J. Geophys. Res. 82, 4826, 1977.

Richmond, A. D. and S. Matsushita, Thermospheric response to a Magnetic Substorm", J. Geophys. Res. 80, 2839, 1975.

Testud, J., Gravity waves generated during magnetic substorms, J. Atmos. Terr. Phys. 32, 1793, 1970.

Waco, D. E., A statistical analysis of wind and temperature variables associated with high altitude clear air turbulence (HICAT), J. Appl. Meteor. 9, 300, 1970.

Wilson, C. R., Infrasonic wave generation by aurora, J. Atmos.
Terr. Phys. 37, 973, 1975.

Woods, J. D., On Richardson's number as a criterion for laminar-
turbulent-laminar transition in the ocean and atmosphere, Radio
Sci. 4, 1289, 1969.

LABORATORY OPERATIONS

The Laboratory Operations of The Aerospace Corporation is conducting experimental and theoretical investigations necessary for the evaluation and application of scientific advances to new military space systems. Versatility and flexibility have been developed to a high degree by the laboratory personnel in dealing with the many problems encountered in the nation's rapidly developing space systems. Expertise in the latest scientific developments is vital to the accomplishment of tasks related to these problems. The laboratories that contribute to this research are:

Aerophysics Laboratory: Launch vehicle and reentry aerodynamics and heat transfer, propulsion chemistry and fluid mechanics, structural mechanics, flight dynamics; high-temperature thermomechanics, gas kinetics and radiation; research in environmental chemistry and contamination; cw and pulsed chemical laser development including chemical kinetics, spectroscopy, optical resonators and beam pointing, atmospheric propagation, laser effects and countermeasures.

Chemistry and Physics Laboratory: Atmospheric chemical reactions, atmospheric optics, light scattering, state-specific chemical reactions and radiation transport in rocket plumes, applied laser spectroscopy, laser chemistry, battery electrochemistry, space vacuum and radiation effects on materials, lubrication and surface phenomena, thermionic emission, photosensitive materials and detectors, atomic frequency standards, and bioenvironmental research and monitoring.

Electronics Research Laboratory: Microelectronics, GaAs low-noise and power devices, semiconductor lasers, electromagnetic and optical propagation phenomena, quantum electronics, laser communications, lidar, and electro-optics; communication sciences, applied electronics, semiconductor crystal and device physics, radiometric imaging; millimeter-wave and microwave technology.

Information Sciences Research Office: Program verification, program translation, performance-sensitive system design, distributed architectures for spaceborne computers, fault-tolerant computer systems, artificial intelligence, and microelectronics applications.

Materials Sciences Laboratory: Development of new materials: metal matrix composites, polymers, and new forms of carbon; component failure analysis and reliability; fracture mechanics and stress corrosion; evaluation of materials in space environment; materials performance in space transportation systems; analysis of systems vulnerability and survivability in enemy-induced environments.

Space Sciences Laboratory: Atmospheric and ionospheric physics, radiation from the atmosphere, density and composition of the upper atmosphere, aurorae and airglow; magnetospheric physics, cosmic rays, generation and propagation of plasma waves in the magnetosphere; solar physics, infrared astronomy; the effects of nuclear explosions, magnetic storms, and solar activity on the earth's atmosphere, ionosphere, and magnetosphere; the effects of optical, electromagnetic, and particulate radiations in space on space systems.